



## Compressive failure and kink-band formation modeling

Downloaded from: <https://research.chalmers.se>, 2024-03-13 06:06 UTC

Citation for the original published paper (version of record):

Larsson, R., Brambati, G., Gutkin, R. (2023). Compressive failure and kink-band formation modeling. *European Journal of Mechanics, A/Solids*, 99.  
<http://dx.doi.org/10.1016/j.euromechsol.2023.104909>

N.B. When citing this work, cite the original published paper.



# Compressive failure and kink-band formation modeling

Ragnar Larsson<sup>a,\*</sup>, Giovanni Brambati<sup>c</sup>, Renaud Gutkin<sup>b,a</sup>

<sup>a</sup> Div of Material and Computational Mechanics, Chalmers University of Technology, SE-412 96 Gothenburg, Sweden

<sup>b</sup> Volvo Car Corporation, SE-405 31, Gothenburg, Sweden

<sup>c</sup> Dipartimento di Meccanica, Politecnico di Milano, Via La Masa 1, Milano 20156, Italy

## ARTICLE INFO

### Keywords:

Composites  
Homogenization  
Continuum damage  
Non-local damage  
Fiber kinking

## ABSTRACT

To increase the use of polymeric structural composites, a major issue is to properly account for intra-laminar failure mechanisms, such as fiber kinking induced under compression. We propose a new continuum damage model that can predict the fiber kinking response at the ply level. The model is based on a previous structure tensor-based model for the response of UD-ply. A novel feature is that the compressive UD-ply response at the macroscale includes the effect of the fiber misalignment shaped as a kink-band that is resolved at the sub-scale. Concepts of computational homogenization are used to include the fiber-shear of the kink-band at the sub-scale. The model calibration is adapted to account for either kink-band formation or shear-splitting depending on the off-axis loading. Finally, the model is validated at the laminate level against experimental data for OHC-tests available in the literature. A good agreement is found for predicted strength values and observed fracture patterns of the laminates. The size effect experienced when different hole sizes are tested is also addressed.

## 1. Introduction

Our understanding of the involved mechanisms of longitudinal compressive failure is pivotal for bearing failure and crash simulations in structural Carbon Fiber Reinforced Plastics (CFRP). A major issue for modeling and simulation is to properly account for intra-laminar failure mechanisms, such as fiber kinking typically induced in compression. The instability associated with fiber kinking considered as an effect of the transverse isotropy in UD-ply, cf. Fig. 1, has been studied since long by many researchers, e.g. Fleck et al. (1995)–Jensen and Christoffersen (1997).

It has been shown that compressive failure in fiber reinforced composites arises from large rotation of fibers, also named fiber kinking failure. The failure is promoted by initially misaligned fibers coupled to heavy shear straining of the matrix, as discussed by Fleck et al. (1995) and Pimenta et al. (2009). Fiber kinking may also occur for straight fibers subjected to (slight) off-axis compressive load. Recent studies have investigated fiber kinking based on micro-mechanical models both experimentally and theoretically. However, a major issue is to properly represent the initiation and propagation of kink-bands in a computationally efficient way. Continuum damage models are often used for FE analysis, e.g. Pinho et al. (2014) presented a model based on smeared crack modeling. More recently Gutkin et al. (2016) presented a model accounting for damage growth during fiber kinking in a mechanistic fashion. This model was further developed by Costa et al. (2017) to

obtain mesh objectivity. For large elements a snap-back was observed in the structural response, resulting in numerical difficulties. Some of the drawbacks of this approach are addressed in Leone (2015) to eliminate spurious secondary failure modes. An additional development of this model was made by Herraes et al. (2018) by introducing a decomposition of the deformation gradient into two parts: one related to the kink-band region and one related to the undamaged region. In Larsson et al. (2018), a new set of continuum damage models (both local and non-local gradient damage) were developed to predict fiber kinking response. It was shown that fiber kinking can be resolved without any special built-in feature to include effects of fiber misalignment. Hence, the models in Larsson et al. (2018) strongly supports that fiber kinking is also an effect of fiber off-axis compressive load.

Herein, we propose a formulation based on computational homogenization to describe the effects of initial misalignment of the predominant fiber orientation of a UD-ply, cf. Wilhelmsson et al. (2018). In order to derive the homogenized response of the deformation process in a Representative Volume Element (RVE), the principle of virtual work equivalence is exploited as in the basic Suquet (1985), Miehe et al. (1999). In this approach, the overall fiber orientation of the UD-ply is realized at the macro (=engineering) scale, whereas the fiber misalignment is resolved at the sub-scale. The ply-response at the subscale is represented by the newly developed continuum damage model (Larsson et al., 2018), based on elastic damage exploiting (local)

\* Corresponding author.

E-mail address: [ragnar@chalmers.se](mailto:ragnar@chalmers.se) (R. Larsson).

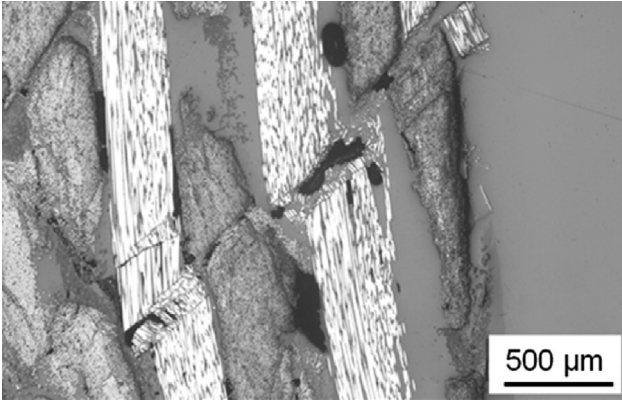


Fig. 1. A micro-graph of a kink band involving compressive failure through several bundles with intermediate matrix cracking, from Grauers et al. (2014).

rate-dependent damage evolution to achieve mesh independence. The model has been implemented into the Abaqus™/Explicit FE-code. Inter-laminar delamination failure is also implemented in the FE-model using Cohesive Zone (CZ) elements available in Abaqus™. Numerical predictions of the load–displacement behavior, as well as damage propagation and failure of OHC-tests are presented and assessed.

## 2. Intra-laminar response of compressive loaded plies

In this section a model for the intra-laminar failure in compression of a UD-ply based on an elastic-damage model is described. The main idea is to establish the transversely isotropic continuum response with the fiber misalignment embedded. To account for the fiber misalignment, a Representative Volume Element (RVE) of the initially misaligned UD-ply is shown in Fig. 2(a). The main fiber orientation of the RVE is defined by the unit normal vector  $\mathbf{N}_\pm$  and the fiber misalignment is represented by the orientation vector  $\mathbf{N}_b$ . The misalignment angle  $\theta$  is then  $\cos \theta = \mathbf{N}_\pm \cdot \mathbf{N}_b$  as shown in Fig. 2(b). A perfect UD-ply is defined by  $\theta = 0$  with  $\mathbf{N}_\pm = \mathbf{N}_b$ . In practice, the initial fiber orientation is considered in terms of a given e.g. periodic distribution of  $\mathbf{N}_b$  over the UD-ply.

### 2.1. Embedded kink band model derived from homogenization

In order to embed the effect of a kink-band in the constitutive response, homogenization of the mechanical behavior of the UD-ply for an initial fiber misalignment is developed. To this end, the RVE in Fig. 2(a), containing the embedded fiber misalignment of width  $k$ , is considered. The RVE has the undeformed 3D domain  $D_\square$ , the volume is  $V_\square = l^2 \times t$  ( $t$  is the thickness), and it is subjected to a constant macroscopic Lagrange strain  $\bar{\mathbf{E}}$  in  $D_\square$  defined as

$$\bar{\mathbf{E}} = \frac{1}{2} (\bar{\mathbf{F}}^t \cdot \bar{\mathbf{F}} - \mathbf{1}), \quad \bar{\mathbf{F}} = \mathbf{1} + \bar{\mathbf{u}} \otimes \nabla_X \quad (1)$$

where  $\bar{\mathbf{F}}$  is the deformation gradient, corresponding to a linearly varying displacement field  $\bar{\mathbf{u}}$  at the macro-level; a bar  $\bar{\cdot}$  is (and will be) used to denote macroscopic quantities.

To represent the local strain field  $\mathbf{E}$  in  $D_\square$ , it is assumed that the strain consists of the constant (applied) part  $\bar{\mathbf{E}}$  and a subscale portion  $\bar{\mathbf{E}}_s$  representing kink-band fiber shear straining in  $D_\square$ . The subscale portion is defined as

$$\bar{\mathbf{E}}_s := a \mathbf{I}_s : \bar{\mathbf{E}} \quad (2)$$

where  $a \in D_\square$  is a scalar field representing the local variation of the subscale fiber shear, and  $\mathbf{I}_s$  is the fourth order tensor that projects the

macro-strain  $\bar{\mathbf{E}}$  into pure fiber shearing  $\mathbf{E}_s$ . Following Larsson et al. (2018), the fiber shear strain projection operator is

$$\mathbf{I}_s = \frac{1}{2} (\mathbf{M} \otimes \mathbf{1} + \mathbf{1} \otimes \mathbf{M}) - \mathbf{M} \otimes \mathbf{M} \quad (3)$$

where  $\mathbf{M} = \mathbf{N} \otimes \mathbf{N}$  is the structure tensor of the fiber orientation. The fiber shear is thus related to the fiber orientation as

$$\bar{\mathbf{E}}_s = \frac{1}{2} (\bar{\mathbf{E}} \cdot \mathbf{M} + \mathbf{M} \cdot \bar{\mathbf{E}}) - (\mathbf{M} : \bar{\mathbf{E}}) \mathbf{M} \quad (4)$$

whereby the local strain field  $\mathbf{E}[\bar{\mathbf{E}}, a] = \bar{\mathbf{E}} + \bar{\mathbf{E}}_s[a]$  in  $D_\square$  is given by

$$\mathbf{E} = \bar{\mathbf{E}} + a \underbrace{\mathbf{I}_s : \bar{\mathbf{E}}}_{\bar{\mathbf{E}}_s} \in D_\square \Rightarrow \delta \mathbf{E} = (\mathbf{I} + a \mathbf{I}_s) : \delta \bar{\mathbf{E}} + \bar{\mathbf{E}} \delta a \in D_\square \quad (5)$$

Here,  $\mathbf{I}$  is the fourth order identity tensor

The Hill–Mandel condition states that the homogenized virtual work equals the virtual work done by the micro-strain and micro-stress fields in the RVE domain. In view of (5), this is formulated in terms of the Lagrange strain and the second Piola Kirchhoff stress  $\mathbf{S}$  as

$$\delta \bar{\mathbf{E}} : \bar{\mathbf{S}} = \delta \bar{\mathbf{E}} : \underbrace{\langle (\mathbf{I} + a \mathbf{I}_s) : \mathbf{S} \rangle_{D_\square}}_{\mathbf{S}} + \underbrace{\bar{\mathbf{E}} : \mathbf{I}_s : \langle \delta a \mathbf{S} \rangle_{D_\square}}_{=0} \quad \forall \delta a \quad (6)$$

where the volume mean of  $D_\square$  is defined through  $V_\square \langle \cdot \rangle_{D_\square} = \int_{D_\square} \cdot d\mathbf{B}$ .

The Hill–Mandel relation in (6) yields the homogenized stress

$$\bar{\mathbf{S}} = \langle (\mathbf{I} + a \mathbf{I}_s) : \mathbf{S} \rangle_{D_\square} \quad (7)$$

corresponding to micro-mechanical equilibrium represented by

$$\bar{\mathbf{E}} : \mathbf{I}_s : \langle \delta a \mathbf{S}[a] \rangle_{D_\square} = \bar{\mathbf{E}}_s : \langle \delta a \mathbf{S}[a] \rangle_{D_\square} = 0 \quad \forall \delta a \quad (8)$$

We also consider the corresponding kinematic compatibility condition stating that the local scalar field  $a$  has a vanishing mean in the RVE domain, i.e.

$$\langle \delta \bar{\mathbf{S}} : (a \mathbf{I}_s : \bar{\mathbf{E}}) \rangle_{D_\square} = \delta \bar{\mathbf{S}} : \mathbf{I}_s : \bar{\mathbf{E}} \langle a \rangle_{D_\square} = 0 \Leftrightarrow \langle a \rangle_{D_\square} = 0 \quad (9)$$

#### 2.1.1. Application to a kink-band formation problem

For the kink-band modeling, the fluctuation  $\bar{\mathbf{E}}_s$  is a pure shear strain relative to the misaligned fiber orientation, i.e. we set  $\mathbf{N} := \mathbf{N}_b$  in (4) to evaluate  $\bar{\mathbf{E}}_s$ . Hence, shearing of the kink-band is locally enhanced by  $\bar{\mathbf{E}}_s[a] := a \bar{\mathbf{E}}_s$ , where  $\bar{\mathbf{E}}_s$  is the macroscopic pure shear strain tensor related to the misaligned fiber and  $a$  is the scalar shear strain field. It is assumed (as also alluded to in Fig. 2(a)) that the stress and strain fields are piece-wise constant in  $D_\square$  so that

$$a = \begin{cases} a_b & \mathbf{X} \in D_\square^b \\ a_\pm & \mathbf{X} \in D_\square^\pm \end{cases}, \quad \mathbf{S} = \begin{cases} \mathbf{S}_b & \mathbf{X} \in D_\square^b \\ \mathbf{S}_\pm & \mathbf{X} \in D_\square^\pm \end{cases} \quad (10)$$

The kinematic compatibility condition (9) yields the consequent piece-wise constant scalar field  $a$  as

$$\int_{D_\square} a d\mathbf{B} = \phi_\pm a_\pm + \phi_b a_b = 0 \Rightarrow a_\pm = -\frac{\phi_b}{\phi_\pm} a_b \quad (11)$$

where  $\phi_\pm$  is the volume fraction of straight fibers and  $\phi_b$  is the volume fraction of misaligned fibers. They have the relation  $\phi_\pm + \phi_b = 1$ .

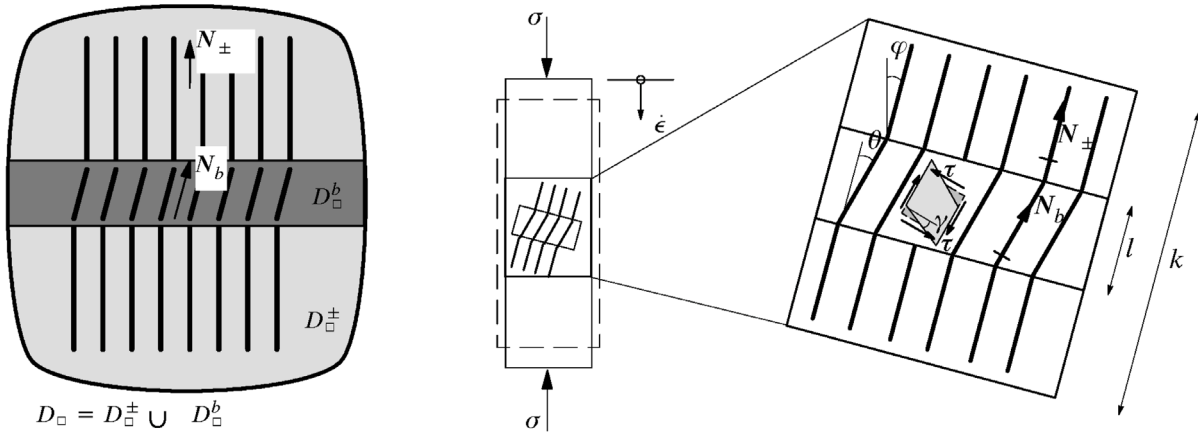
With the assumption about piecewise constant fields, the micro-mechanical equilibrium problem (8) directly reduces to the projection problem

$$\delta a_b \phi_b \bar{\mathbf{E}}_s : (\mathbf{S}_b[a_b] - \mathbf{S}_\pm[a_\pm]) = 0 \quad (12)$$

representing shear stress continuity in the projected sense across the regions of straight and misaligned fibers in the RVE.

We also find that the homogenized (continuum) stress in (7) is obtained explicitly as

$$\bar{\mathbf{S}} = \langle (\mathbf{I} + a \mathbf{I}_s) : \mathbf{S} \rangle_{D_\square} = \phi_\pm \mathbf{S}_\pm + \phi_b \mathbf{S}_b + a_b \phi_b \mathbf{I}_s : (\mathbf{S}_b - \mathbf{S}_\pm) \quad (13)$$



(a) Planar RVE of thickness  $t$  with misaligned fiber orientation. The main fiber direction is  $N_{\pm} \neq N^b$  in  $D_{\pm}$ , whereas  $N^b = N$  represents the misalignment orientation in  $D_b^b$ . In the uniaxial test, an off-axis angle  $\varphi$  and the (initial) misalignment angle  $\theta$  are introduced in the fiber geometry. The fiber shear stress is  $\tau$  and the fiber shear strain is  $\gamma$ .

Fig. 2. RVE  $D_{\square}$  with misaligned fibers in  $D_b^b$  and straight fibers in  $D_{\pm}$ . The main fiber direction is  $N_{\pm} \neq N^b$  in  $D_{\pm}$ , whereas  $N^b = N$  represents the misalignment orientation in  $D_b^b$ . In the uniaxial test, an off-axis angle  $\varphi$  and the (initial) misalignment angle  $\theta$  are introduced in the fiber geometry. The fiber shear stress is  $\tau$  and the fiber shear strain is  $\gamma$ .

## 2.2. Transverse elastic damage response of a UD-ply

A pure transversely isotropic elastic response is assumed for the UD-ply. The total response is given by the effective (undamaged) stored free energy  $\hat{\psi}$ , subdivided into four stored free energy contributions defined as

$$\hat{\psi} = \hat{\psi}^d + \hat{\psi}^v + \hat{\psi}^s + \hat{\psi}^f \quad (14)$$

Upon assuming small strains for the composite while allowing for geometrical non-linearity, the deviatoric strain- and the volume change energies,  $\hat{\psi}^d$  and  $\hat{\psi}^v$ , respectively, are defined in terms of the Lagrange strain as

$$\hat{\psi}^d = \frac{1}{2} 2GE_d : E_d, \quad \hat{\psi}^v = \frac{1}{2} K(1 : E)^2 \quad (15)$$

Here,  $E_d$  is the deviatoric part of  $E$ ,  $G$  is the shear modulus and  $K$  is the bulk modulus of the composite.

As to longitudinal fiber shear and axial fiber actions of the ply-composite, the stored free energies  $\hat{\psi}^s$  and  $\hat{\psi}^f$  are defined as

$$\hat{\psi}^s = \frac{1}{2} G^f (\gamma^f)^2 = \frac{1}{2} 2G^f E_s : E_s, \quad \hat{\psi}^f = \frac{1}{2} E^f (\epsilon^f)^2 = \frac{1}{2} E^f (M : E)^2 \quad (16)$$

where  $G^f$  and  $E^f$  are parameters for fiber shear and axial stiffness related to the fiber direction of the ply-composite.

In the constitutive equations above the parameters  $G, K, G^f, E^f$  are related to the tensor based formulation. These parameters relate to the classical ones, often used in composites mechanics, cf. Larsson et al. (2018)

$$K = \frac{E_2}{3(1 - \nu_{23} - 2\xi\nu_{12}^2)} \frac{1 + \xi\nu_{12}^2 + 2\nu_{23}}{1 + \nu_{23}} \quad (17a)$$

$$G = G_{23} = \frac{E_2}{2(1 + \nu_{23})} \quad (17b)$$

$$E^f = \frac{E_1}{1 - \nu_{23} - 2\xi\nu_{12}^2} \frac{1 - \xi + \xi^2\nu_{12}^2 - \nu_{23}^2}{1 + \nu_{23}} \quad (17c)$$

$$G^f = 2(G_{12} - G_{23}) \quad (17d)$$

where  $E_1$  is the modulus of elasticity in the fiber direction,  $\nu_{12}$  is the Poisson's ratio of the matrix-fiber plane,  $G_{12}$  is the longitudinal shear modulus,  $E_2$  is the modulus of elasticity of the isotropy plane,  $\nu_{23}$  is the Poisson's ratio of the isotropy plane and  $G_{23}$  is the shear modulus of the isotropy plane. Finally,  $0 < \xi < 1$  is the ratio  $E_2/E_1$ .

Following the developments in Larsson et al. (2018), the model is formulated so that the damage evolution is driven by matrix- and

longitudinal fiber shear, followed by fiber collapse. This is achieved by a single scalar variable  $0 \leq \alpha \leq 1$  representing the degradation of the UD-fiber reinforced polymer. The degradation is formulated in terms of stored free energy contributions defined as

$$\psi = f[\alpha]\hat{\psi}^d + h[\alpha]\hat{\psi}^s + g[\alpha]\hat{\psi}^f + \hat{\psi}^v \quad (18)$$

where the function  $f[\alpha]$  captures degradation of the matrix shear,  $h[\alpha]$  is responsible for degrading the longitudinal fiber shear response, and the function  $g[\alpha]$  captures the fiber crushing mechanism. These functions define exponential degradation in terms of the exponents  $\beta^f$ ,  $\beta^h$  and  $\beta^g$  defined as

$$f[\alpha] = (1 - \alpha)^{\beta^f}, \quad g[\alpha] = (1 - \alpha)^{\beta^g}, \quad h[\alpha] = (1 - \alpha)^{\beta^h} \quad (19)$$

Due to the evolution of damage, the rate of energy dissipation per unit volume is

$$D := S : \dot{E} - \dot{\psi} = S : \dot{E} - \underbrace{\frac{\partial \psi}{\partial E} \dot{E}}_{=0} - \underbrace{\frac{\partial \psi}{\partial \alpha} \dot{\alpha}}_{\mathcal{A}} \quad \dot{\alpha} = \mathcal{A} \dot{\alpha} \geq 0 \quad (20)$$

corresponding to the state equation for the 2nd Piola Kirchhoff stress

$$S = \frac{\partial \psi}{\partial E} = f[\alpha]\hat{S}^d + g[\alpha]\hat{S}^f + h[\alpha]\hat{S}^s + \hat{S}^v \quad (21)$$

where

$$\hat{S}^d = \frac{\partial \hat{\psi}^d}{\partial E} = 2GE_d \quad (22a)$$

$$\hat{S}^v = \frac{\partial \hat{\psi}^v}{\partial E} = K1(1 : E) \quad (22b)$$

$$\hat{S}^f = \frac{\partial \hat{\psi}^f}{\partial E} = E^f M(M : E) \quad (22c)$$

$$\hat{S}^s = \frac{\partial \hat{\psi}^s}{\partial E} = 2G^f E_s \quad (22d)$$

It may be remarked that the local stresses (inside and outside the kink-band) are evaluated in the local strains/orientations as  $S_b = S[E_b, M_b]$  and  $S_{\pm} = S[E_{\pm}, M_{\pm}]$ . Moreover, the damage driving energy  $\mathcal{A}$  for the process of damage is

$$\mathcal{A} = -\frac{\partial \psi}{\partial \alpha} = -f'[\alpha]\hat{\psi}^d - g'[\alpha]\hat{\psi}^f - h'[\alpha]\hat{\psi}^s \quad (23)$$

where the local damage evolution law in Larsson et al. (2018) is considered. Here, it is assumed that non-negative damage evolution  $\dot{\alpha} > 0$  is controlled by the given finite speed parameter  $v^*$ , whereby the damage

evolution is governed by a Bingham-viscoplastic type model written as

$$l_c \dot{\alpha} = v^*(\alpha^s - \alpha)^+ \text{ with } \alpha^s = \frac{\mathcal{A}[\alpha] l_c}{G_c} \quad (24)$$

where  $(\bullet)^+ = \frac{1}{2}(\bullet + |\bullet|)$  is the positive part function and  $\alpha^s[\alpha]$  represents “static” damage (corresponding to  $v^* \rightarrow \infty$ ) due to elastic deformation. Moreover,  $G_c$  is the fracture energy parameter for the compressive failure and  $l_c$  is the internal length parameter describing a diffuse fracture area. The damage evolution model (24) generally yields mesh-objective response manifested by localized damage zones, whose width is governed by the  $l_c$ -parameter, cf. Larsson et al. (2018).

It may be noted that the damage evolution law in (24) may formally be integrated during a continuous damage loading process with duration  $T$ . This is formulated as

$$\frac{1}{T} \int_0^T d\alpha = \frac{\alpha}{T} = \frac{v^*}{l_c} \left( \frac{\bar{\mathcal{A}} l_c}{G_c} - \bar{\alpha} \right) \quad (25)$$

where  $\bar{\mathcal{A}}$  and  $\bar{\alpha}$  are the mean values of the damage driving force  $\mathcal{A}$  and the damage variable  $\alpha$  during the damage process. These temporal mean values are defined as

$$\bar{\mathcal{A}} = \frac{1}{T} \int_0^T \mathcal{A}[t] dt, \quad \bar{\alpha} = \frac{1}{T} \int_0^T \alpha[t] dt \quad (26)$$

For small relaxation times  $t^*/T = l_c/(v^*T) \ll 1$  we obtain

$$\bar{\mathcal{A}} = \frac{G_c}{l_c} \left( \bar{\alpha} + \alpha \frac{t^*}{T} \right) \approx \frac{G_c}{l_c} \bar{\alpha} \quad (27)$$

whereby the temporal mean of the driving force  $\bar{\mathcal{A}}$  represents the released fracture surface energy  $G_c$  in the diffuse damage zone of width  $l_c$ . Hence, the damage progression speed is chosen large enough to motivate  $l_c \ll v^*T$ , whereas  $l_c$  is chosen with respect to the kink-band width.

### 2.3. Kink-band failure scenario

Consider the uni-axial compression test of the UD-ply, with the fiber misaligned angle  $\theta$  in Fig. 2(b). The micro-structure of the misaligned fiber is given in the close-up, where the periodicity of the misalignment is  $k$  and the internal width of the kink band is  $l$ . For a thin ply it then follows that

$$\phi_b = \frac{kl}{k^2} = \frac{l}{k}, \quad \phi_{\pm} = 1 - \phi_b \Rightarrow a_{\pm} = -\frac{\phi_b}{\phi_{\pm}} a_b = -\frac{\frac{l}{k}}{1 - \frac{l}{k}} a_b \quad (28)$$

Hence, the homogenized response depends on the  $l/k$ -ratio, rather than on the explicit dependence of  $k$  and  $l$ . For the presence of a kink-band it is assumed that damage degradation is localized to  $D_{\square}^b$  (with the kink band width  $l_c$  as alluded to in (24)), whereas pure elastic response takes place in  $D_{\square}^{\pm}$ . In order to obtain the scalar parameter  $a_b$ , the scalar shear stress continuity condition (12) is solved using a Newton iteration procedure along with a check of the assumed loading condition. For kink-band development the internal length in the damage progression (24) is assumed to be in the order of the kink-band width, i.e.  $l \approx l_c$  in Fig. 2(b). Hence, for kink-band development, damage is regarded as an internal macro-variable that is degrading the response in  $D_{\square}^b$ .

However, note that the “kink-band mode” is not the only mode present during compressive failure. It appears that kink-bands are activated for small off-axis angles  $\varphi \leq 10^\circ$ , cf. Fig. 2(b). For off-axis angles  $\varphi > 10^\circ$  compressive matrix shear failure predominates. This is manifested by a mode I splitting mechanism, named shear-splitting, at the micro-level. In the latter case the effect of the misalignment is negligible. To handle this situation, we set  $l = k$  (or  $\phi_b = 1$ ),  $N_b = N_{\pm}$  and  $a_b = a_{\pm} = 0$ , corresponding to the homogenized response governed by the macroscopic strain  $E_b = \bar{E}$ . The consequences of this behavior is further discussed in sub-Section 3.1, related to the calibration of the damage-model parameters.

**Table 1**

Elastic parameters of the considered UD-ply.

$E_1$ GPa	$E_2$ GPa	$\nu_{12}$	$G_{12}$ GPa	$\nu_{23}$
163	9.08	0.32	5.29	0.46

### 3. Representative numerical examples

This section describes the model parameter calibration and numerical results coming from the finite element simulations of the model. Simulations of uniaxial compression tests of a ply specimen at the material point level, and at the FE level, are carried out for experimental calibration and validation. Finally, Open Hole Compression (OHC) tests for laminates with different sizes are presented and compared to the corresponding experimentals available in the literature.

The model implementation has been made in Abaqus/Explicit, where the material model is defined as a VUMAT-subroutine, (Smith, 2009). Mass scaling is used to handle the quasi-static condition, where the material density is artificially increased to allow for an increase the time step  $\Delta t$ . It is activated so that the mass is increased only if the time increment is below the threshold  $10^{-6}$ s. Moreover, the kinetic energy of the structure is monitored to keep it relatively low compared to the applied external work. Mass scaling and load-stepping are carefully controlled in order not to have kinematic components higher than 10% of the external work.

#### 3.1. Model calibration and validation for a uniaxial compression test

Since the UD-ply exhibits kink-band or shear-splitting failure modes, two separate calibrations of the damage parameters involved in (24) are performed. The elastic ply-properties are the same for all of the ply-specimens considered, cf. Table 1. For the kink-band failure mechanism, the damage parameters are calibrated using the fiber shear stress  $\tau^f = h[\alpha] \frac{\partial w^f}{\partial \gamma^f} = h[\alpha] G^f \gamma^f$ . The shear stress is fitted to the experimental shear stress curve from Gutkin et al. (2016) for a  $0^\circ$  loaded UD-ply with the misalignment angle  $\theta = 5^\circ$ . The results from the calibration of the shear response is shown in Fig. 3(a), corresponding to the damage parameters in Table 2. The consequent brittle compressive uniaxial response is given in Fig. 3(b).

Concerning the shear-splitting failure (for  $\varphi > 10^\circ$ ), the calibration of the damage parameters are considered against the quasi-static off-axis experimental results in Koerber and Camanho (2011). In this case the kink-band width  $l$  is the RVE width  $k = 2.4$  mm, cf. Table 2, corresponding to a more diffuse damage region as compared to the kink-band case. As alluded to in Section 2.3, the model response is represented by the elastic-damage model governed by  $\bar{E}$  without any kink-band enhancement. Moreover, due to the fact that the OHC-test specimens considered later have only  $0^\circ$ ,  $\pm 45^\circ$  and  $90^\circ$  fiber orientations, the model is calibrated against the  $\varphi = 45^\circ$  off-axis compression case. (The off-axis angle  $\varphi$  is shown in Fig. 2(b)). The results of the calibration for shear-splitting failure is shown in Table 2 and in Fig. 4. The more ductile behavior as compared to in Fig. 3(b) is noteworthy.

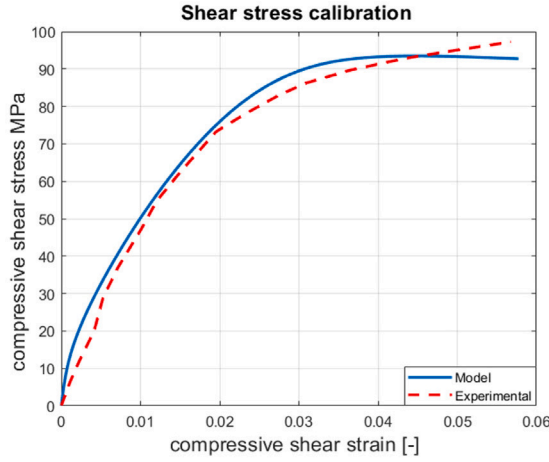
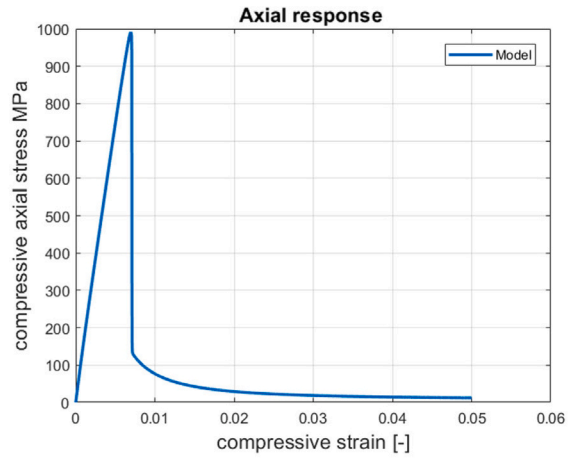
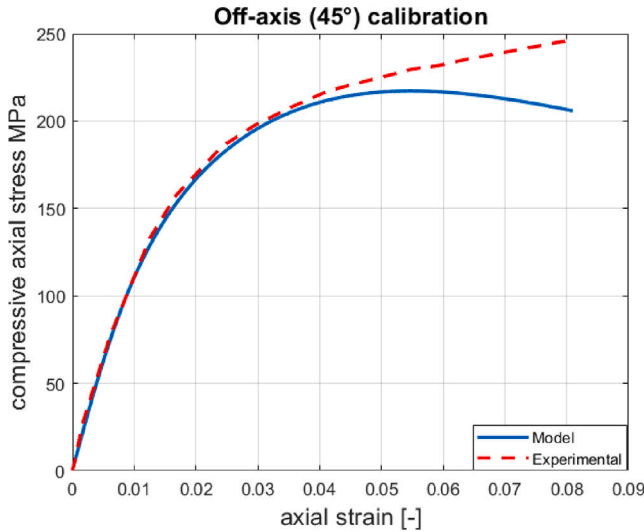
Further validation is made from the shear-splitting failure by using experimental results of the other off-axis cases in uni-axial compression by Koerber and Camanho (2011). Fig. 5 shows the simulation results of the model for the off-axis loading cases:  $15^\circ$ ,  $30^\circ$ ,  $60^\circ$  and  $75^\circ$  as compared to the experimental results. The simulations show a good correspondence with the experimental values for the pre-peak behavior. Note that we have no experimental information on the softening and final failure phase in the uniaxial tests. However, for the behavior post peak, the calibrated fracture energy in compression and kink-band widths in Table 2 are in-line with the corresponding typical data in Bru et al. (2016) and in Larsson et al. (2018).



**Table 2**

Calibrated damage parameters for kink-band and shear splitting failure modes.

Failure mode	$G_c$ [kJ/m <sup>2</sup> ]	$\beta_f$ [-]	$\beta_h$ [-]	$\beta_g$ [-]	$\phi_b = \frac{l}{k}$ [-]	$l_c$ [mm]	$\theta^\circ$
Kind-band	63	6.7	81	38	0.083	0.31	5
Shear-splitting	120	14.8	81	26	1	0.06	0

(a) Fiber shear stress  $\tau^f[\gamma^f]$  against experiment.(b) Compressive uniaxial response for  $0^\circ$  loading. The embedded misalignment angle is  $\theta = 5^\circ$ .**Fig. 3.** (a) Calibration against fiber shear stress for kink-band failure, (Gutkin et al., 2016). (b) Resulting uniaxial compressive model response at the material point level.**Fig. 4.** Model calibration against the axial response of a  $45^\circ$  off-axis loading at material point level, (Koerber and Camanho, 2011).

### 3.2. FE-analysis of UD-ply specimens

In order to evaluate the relation between the structural behavior of the UD-ply and the calibration/validation at the material point level in sub-Section 3.1, FE-analyses of compression tests on UD-ply specimens are carried out. Here, the boundary conditions for the considered UD-ply are defined to mimic the compressive uniaxial stress state, Fig. 6. Here, two elastic regions are introduced to simulate the gripping zone at the tab ends.

The initial unidirectional specimen tested is the one with the fiber orientation parallel to the loading direction, referred to as the  $\varphi = 0^\circ$  off-axis angle. Since we have  $\varphi < 10^\circ$ , kink-band response is diagnosed with the misalignment  $\theta = 5^\circ$ . Fig. 8 shows the deformed structure

(displacement scale exaggerated) at peak-load superimposed with the distribution of the damage variable  $\alpha$  (named *SDVI* in the figure legends). Clearly, we observe that damage localizes into a kink-band through the width of the specimen. The reason why kinking appears to the sides of the faces is the presence of the regions at the ends of the sample where the material shows only elastic properties. From Fig. 7, it is seen that the ultimate strength of the material is close to the one measured by Lee and Soutis (2008). In addition, the response curves in Fig. 7 show that the adopted damage model exhibits mesh objectivity. In the analyses, three different mesh designs, with the element lengths  $l_e = 1$  mm,  $l_e = 0.5$  mm and  $l_e = 0.25$  mm are considered.

Upon comparing Figs. 9 and 4, the uniaxial analysis at the material point level is not completely comparable with the FE-analysis of the UD-specimen. The nonlinear response is satisfactory up to ca 3% axial straining, whereas the post-peak response initiates too early. This is due to the degrading elastic damage evolution and a possible mismatch of the boundary conditions of the specimen in-situ as compared to in the FE-model. The deformation in the form of a diffused shear band is in good agreement with the test in Fig. 10. Indeed, the in plane shear splitting mode observed in the experimental campaign (Koerber and Camanho, 2011) is captured.

Fig. 11 shows the results for the  $30^\circ$  off-axis case. Like in the  $45^\circ$  off-axis case, the model does not capture the full ductility of the specimen. In Fig. 11(b) a shear band with the same orientation of the fiber inclination initiates at the peak stress.

If we further increase the off-axis angle to  $60^\circ$ , it is noted in Fig. 12(a) that the ductility of the response is fairly well captured by the model. However, the axial stress is underestimated. This is expected since in Fig. 5(c) we can see the same tendency. In addition, Fig. 12(b) exhibits band shaped shear-splitting in two shear bands emanating from the stress free edges of the specimen.

The results from the largest off-axis case  $75^\circ$  are presented in Fig. 13. This result is similar to the  $60^\circ$  case with a ductility in-line with the experiment. As to the shear splitting, Fig. 13(b) exhibits the initiation of multiple shear bands emanating from the stress free edges.

For the  $15^\circ$  off-axis case in Fig. 14, the deformed structure exhibits a failure mode that resembles the kink-band in Fig. 8. However, the

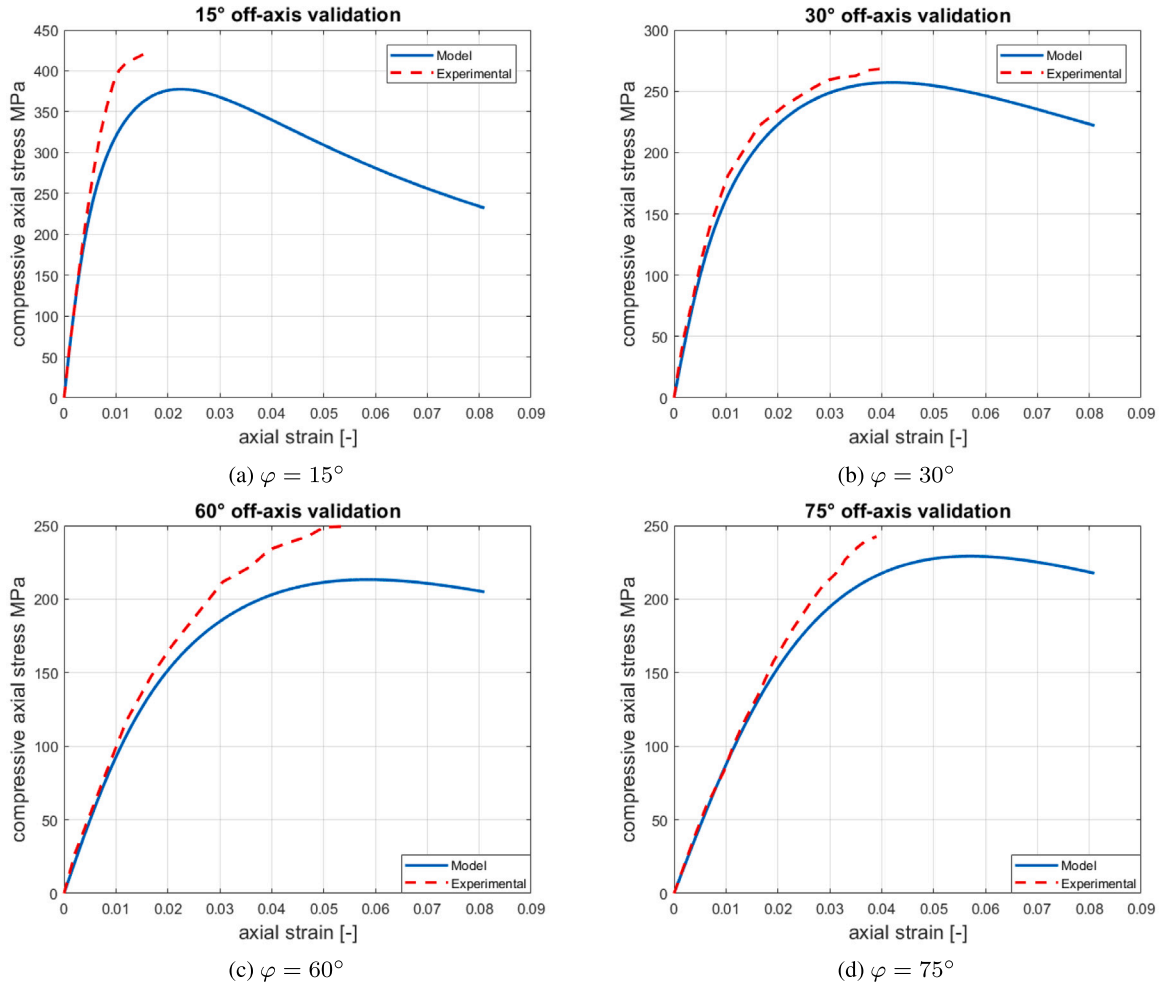


Fig. 5. Validation of uniaxial model response at the material point level against the shear-splitting failure mode for different off-axis loading angles, (Koerber and Camanho, 2011).

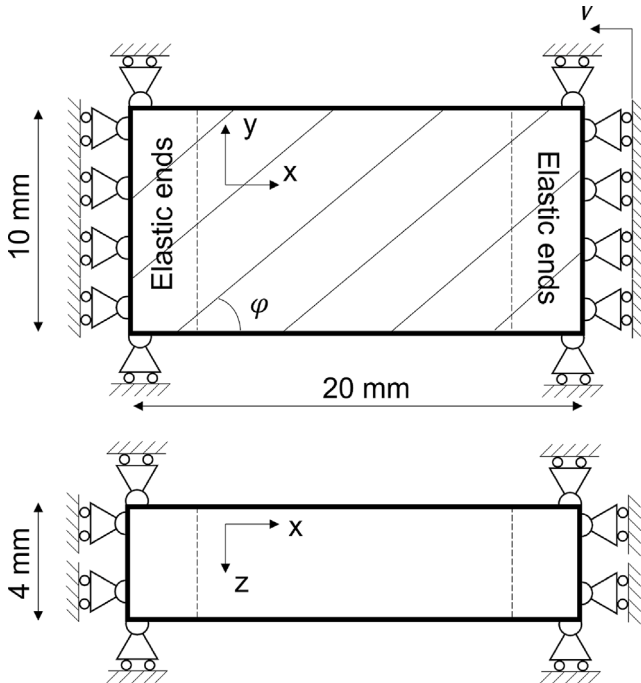


Fig. 6. Considered 3D-geometry and boundary conditions of UD-ply for FE-simulations.

behavior is more ductile with a lowered peak stress as compared to the  $0^\circ$  off-axis case with the embedded kink-bank in Fig. 7. It thus appears that the  $15^\circ$  off-axis case is close to the threshold between kink-band failure and shear-splitting. The shear introduced by the fiber inclination corresponds to a localized kink-band failure rather than in a more diffuse shear-splitting band.

### 3.3. Inter-laminar failure

For the delamination between plies with different fiber orientation, we follow the Cohesive Zone (CZ) model available in Abaqus (Smith, 2009). Here, a (penalized) elastic-damage CZ-formulation is considered in terms of an initial elastic law defined as

$$t = (1 - D)\hat{t}, \quad \hat{t} = \mathbf{K} \cdot \delta \quad \text{and} \quad \mathbf{K} = k\mathbf{1} \quad (29)$$

where  $D$  is the interface damage variable,  $t$  is the nominal traction stress vector (with components  $t_n, t_s, t_t$ ) across the CZ. The corresponding displacement discontinuity (or ply-separation) vector across the CZ is denoted  $\delta$ , with the components  $\delta_n, \delta_s, \delta_t$ . Damage initiation is predicted using a quadratic stress-based criterion:

$$\left( \frac{\max(0, t_n)}{t_n^0} \right)^2 + \left( \frac{t_s}{t_s^0} \right)^2 + \left( \frac{t_t}{t_t^0} \right)^2 = 1 \quad (30)$$

where  $t_n^0, t_s^0, t_t^0$  are the peak values of the contact stress when the separation is either purely normal to the interface or purely in the first or the second shear direction. Once the damage is initiated, damage

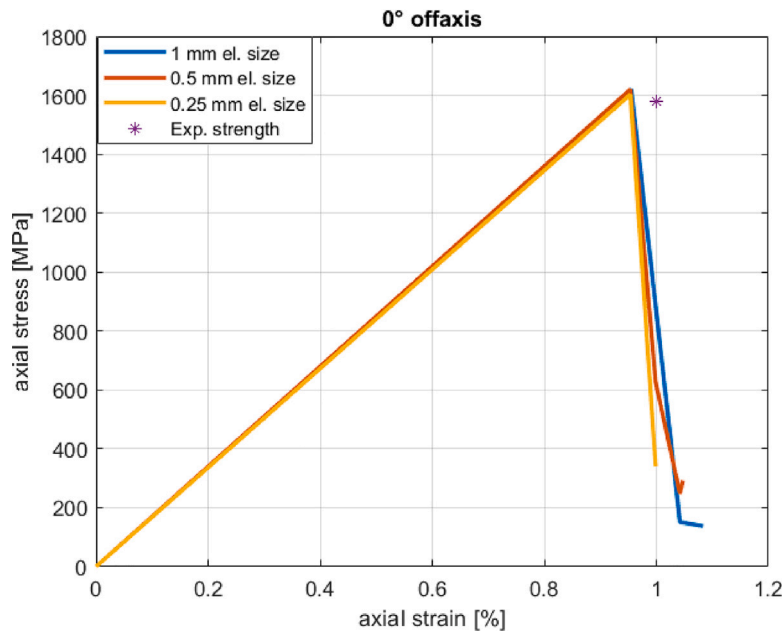


Fig. 7. Axial stress–strain response from FE-ply analysis for the 0° off-axis case. The ultimate compressive strength is from Lee and Soutis (2008).

Table 3

Parameters of the Abaqus mixed-mode traction–separation cohesive interaction used to model inter-laminar failure.

$\hat{k}$ [N/mm <sup>3</sup> ]	$t_n^0$ [MPa]	$t_s^0, t_t^0$ [MPa]	$G_n^c$ [kJ/m <sup>2</sup> ]	$G_s^c, G_t^c$ [kJ/m <sup>2</sup> ]	$\eta$ [–]
$10^6$	60	90	0.28	0.79	1.75

progression is determined under mixed-conditions with the delamination fracture energies  $G_n, G_s, G_t$ . From these parameters introduced by the user, the total toughness is  $G_T = G_n + G_s + G_t$  and the portion of the total work done by the shear traction  $G_S = G_s + G_t$ . A semi-empirical B-K criterion is used where damage progression is computed finding the value of the energy dissipated due to failure ( $G^C$ ).

$$G^C = G_n^C + (G_s^C - G_n^C) \left( \frac{G_S}{G_T} \right)^\eta \quad (31)$$

where  $\eta$  is the exponential model parameter defined experimentally in Benzeggagh and Kenane (1996). The parameters used in the analysis can be seen in Table 3. Details of the damage evolution law may be found in Smith (2009) and in Camanho and Davila (2002).

The choice of the stiffness coefficient (or penalty parameter)  $\hat{k}$  of the  $\mathbf{K}$  matrix has a significant effect on the solution. A too low value leads to an inaccurate representation of CZ, whereas a too high value promotes numerical errors and overly demanding computational effort. The optimum value for the penalty parameter is the largest value that do not lead to numerical problems. Based on Chen et al. (2013), we choose  $\hat{k} = 10^6$  N/mm for all the components. Moreover, the presence of a CZ requires additional considerations of the selected element size. Different models have been proposed in the literature to estimate the length of the CZ. In the work of Turon et al. (2007), a summary of models are presented alongside an evaluation of the mesh element size to correctly capture delamination. In this case, it turns out that a mesh size of 0.5 mm is required for the proper convergence of the results.

### 3.4. Open hole compression test

Following the guidelines specified in ASTM D6484 for an OHC-test, the specimen in Fig. 15 is considered. Like in the physical tests, failure should occur close to the center section of the coupon. To assure

this, an area at each end of the test specimen is modeled as elastic without damage progression. In Fig. 15, these areas are indicated by a blue dotted line. For the tests with the specimen thickness is 2 mm, an additional boundary condition to prevent displacement in the  $y$ -direction is added. This is necessary to mimic the anti-buckling guides used in these cases. The compression applied by the testing machine is modeled using a prescribed velocity on the specimen end that is not fixed. The velocity is assumed constant, except at the very beginning of the analysis where it is smoothed up in order not to introduce un-physical accelerations.

From the experimental work by Wisnom et al. (2010), the laminated (angle-ply) specimen is of the type  $[45_m/90_m/-45_m/0_m]_nS$ , where  $m$  and  $n$  represent two different types of scaling the thickness. Sub-laminate scaling is the stacking when the sequence is repeated  $n$  times with a single ply of each orientation. The other type of stacking is ply-scaling, where blocks of  $m$  plies of the same orientation are stacked together. In the present paper we are focusing on the sub-laminate scaling. The stacking layup is presented in Fig. 16(c) and the single ply has a thickness of 0.125 mm. In addition, specimens with different hole dimensions are analyzed. In order to keep constant (elastic) stress concentration factors, the ratio between the specimen width and the hole diameter is equal to five.

A coupon is formed by sub-laminate scaling, where each ply has separate properties and fiber orientation. The resulting coupon is composed of eight node brick elements, where each ply has the thickness 0.125 mm. Three different cases with symmetric  $[45/90/-45/0]$  sequences of sub-laminate scaling are considered: a 2 mm thick laminate with 4\*4 plies, a 4 mm thick laminate with 4\*8 plies, and a 8 mm thick laminate with 4\*16 plies. The mesh design is governed by the ply-stacking, where the in-plane element dimension is constrained by one element per ply in the thickness direction of the laminate. Like in the meshing in Zhou et al. (2017), partitions are made to have a structured mesh in presence of the hole as shown in Fig. 16(a). Related to the



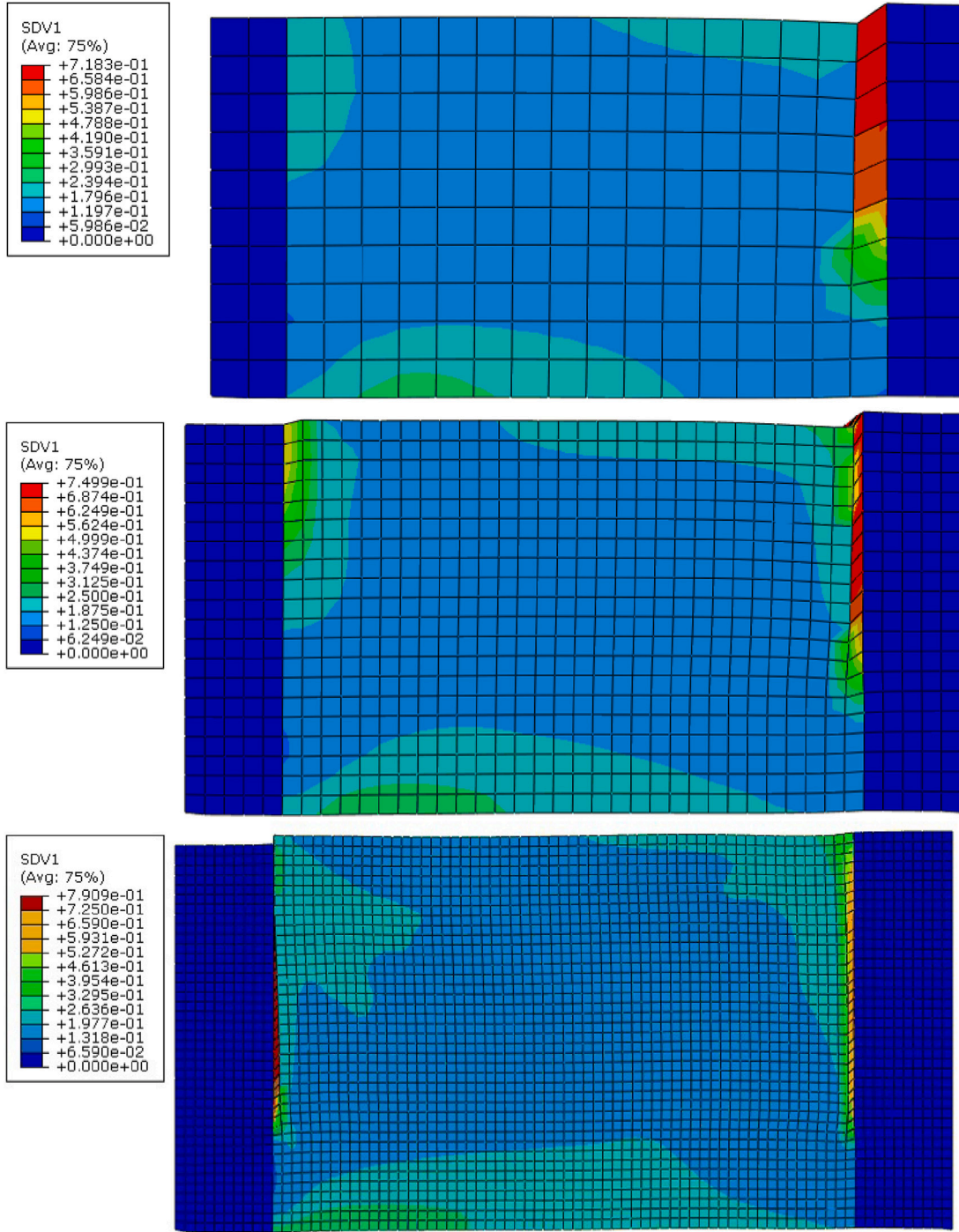


Fig. 8. Sequence of deformed meshes of the UD-ply at peak-load for the  $\varphi = 0^\circ$  off-axis case. SDV1 is the damage variable  $\alpha$ .

resolution of the CZ-traction  $t$  and the progression of delamination, the CZ-interaction between plies imposes requirements on the element size. To maintain control of the explicit solution procedure, the adopted element type *C3D8R* combines a reduced 1-point integration formulation with hourglass control. It is always verified in the simulations that the artificial energy introduced is negligible compared to the external work applied to the system. Different meshes with element lengths  $\leq 0.5$  mm are tested for the sub-laminate scaled specimen with the total thickness 2 mm. The results of the tests can be seen in Fig. 16(b). Since the predicted peak-stress variation is negligible, we choose a mesh size of 0.5 mm for our FE-analyses. Moreover, in order to handle highly

distorted elements, it is necessary to introduce an element removal strategy based on the element residual strength defined as

$$f_{dam} = (1 - \alpha)^\beta \leq 0.01 \text{ with } \beta = \min\{\beta^f, \beta^s, \beta^h\} \quad (32)$$

If  $f_{dam} < 0.01$ , the element is deleted during the simulation.

With the model for the inter-laminate failure introduced in Section 3.3, we proceed with the analyses of the multi-directional laminated structures. For each stacking sequence, different hole diameters are analyzed, while keeping the specimen width over hole diameter ratio constant and equal to five. In order to validate the material model, the results are compared to the experimental test performed

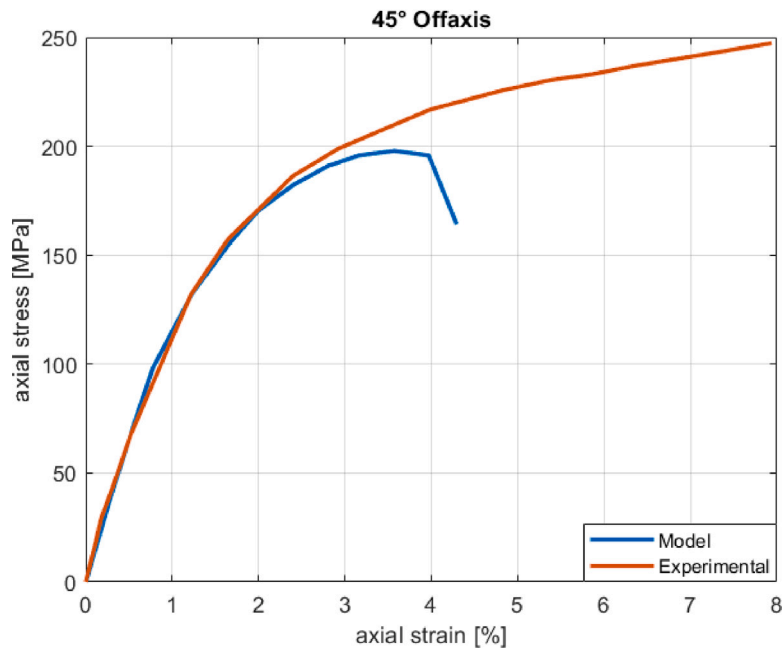
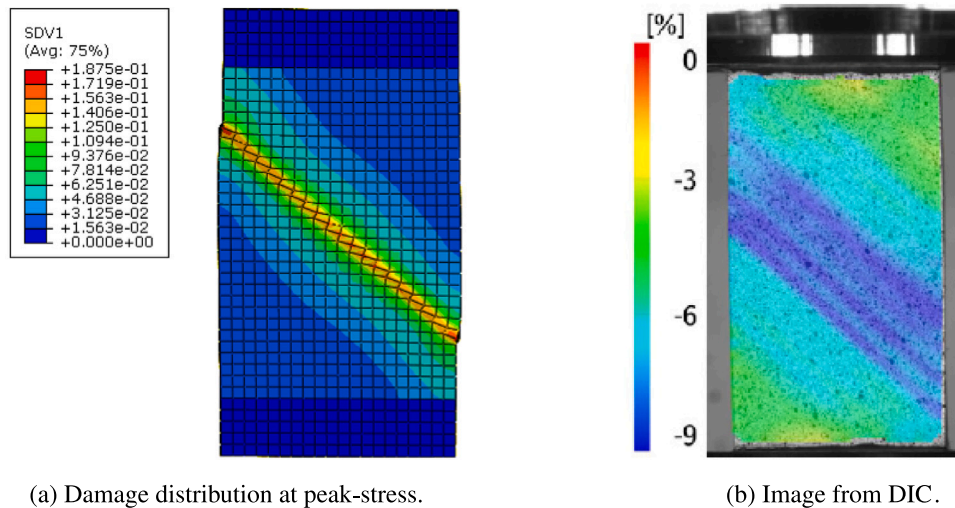


Fig. 9. 45° off-axis stress–strain response from the FE-ply analysis of the compressive test compared to the corresponding the experimental results, (Koerber and Camanho, 2011).



(a) Damage distribution at peak-stress.

(b) Image from DIC.

Fig. 10. (a) Damage distribution from the FE-ply simulation. (SDV1 is the damage variable  $\alpha$ .) (b) axial compressive strain distribution from the experimental test, (Koerber and Camanho, 2011).

Table 4

Strength (MPa) of the sub-laminate scaled specimens. Within parenthesis are the experimental results by Wisnom et al. (2010) with the relative difference.

t [mm]	Sub-laminate scaling			
	Hole diameters [mm]			
	0	6.35	12.7	25.4
2	646 (658) -2%	345 (338) +2%		
4	681 (675) +1%	359 (351) +2%	314 (301) +5%	- (285)
8	658 (644) +2%			- (284)

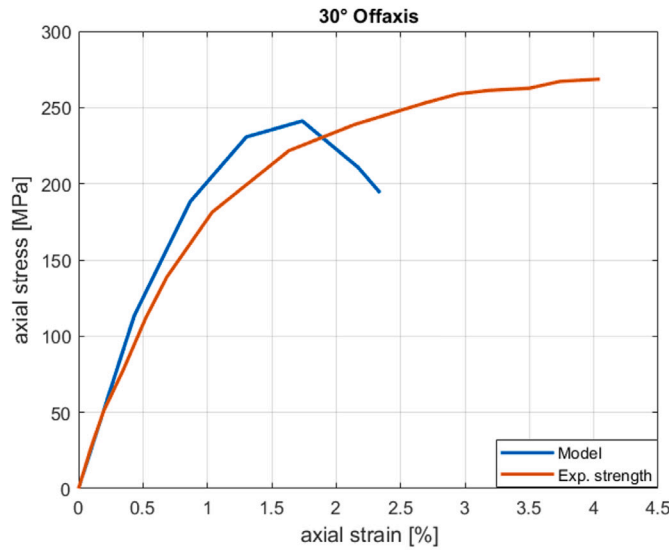
by Wisnom et al. (2010) and Lee and Soutis (2008). The main results of the investigation for the sub-laminate stacking in Fig. 16(c) are summarized in Table 4.

#### 3.4.1. Un-notched specimens

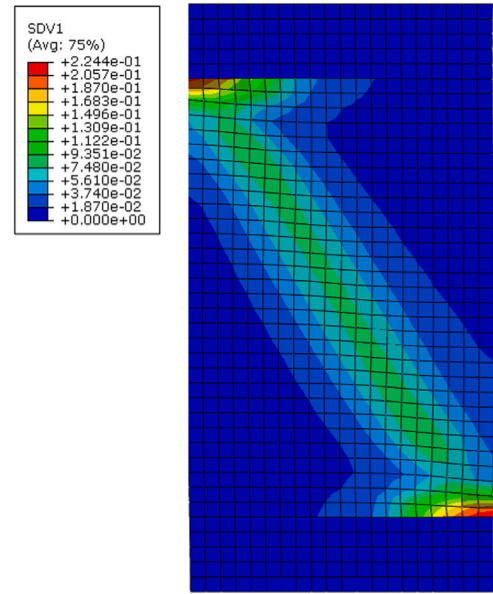
To start with, the results of the compression test for the un-notched specimens are considered. This is the only case where we have experimental results for all three laminate thicknesses. From Table 4, the strength of the un-notched specimens (with sub-laminate scaling) is well captured by the model. The model does not show any significant thickness size dependency as confirmed by Wisnom et al. (2010). All failure mechanisms are similar to those obtained for the 0° UD-specimen, where a kink-band is formed close to the elastic ends. Fig. 17 shows the stress versus axial strain response for the 2 mm thick specimen. The quasi-brittle stress–strain response is similar in the FE-analyses of the other laminate thicknesses.

#### 3.4.2. Notched sub-laminate scaled specimens

Next we consider compression testing of the notched sub-laminate scaled specimens with a hole. The smallest hole diameter available is 6.35 mm, corresponding to a  $32 \times 32 \text{ mm}^2$  size coupon to assure

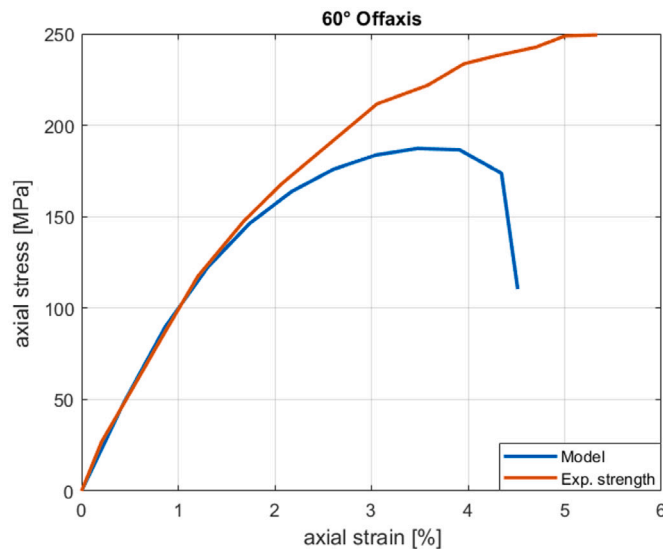


(a) Stress-strain response from FE-analysis.

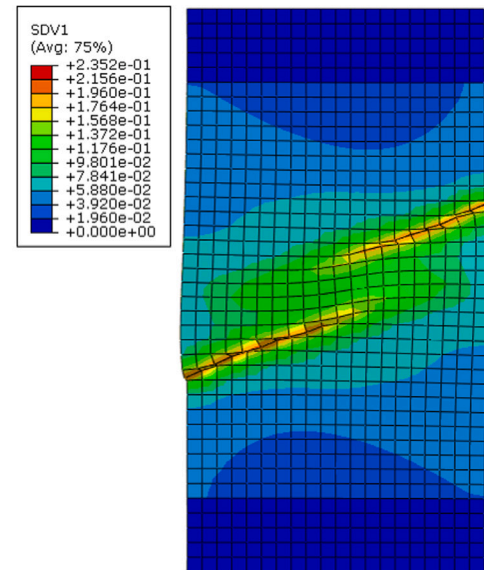


(b) Damage distribution at peak-stress.

**Fig. 11.** (a) FE-analysis of the UD-ply specimen for 30° off-axis loading, (Koerber and Camanho, 2011). (b) Shear-splitting failure mode with damage. (SDV1 is the damage variable  $\alpha$ .)



(a) Stress-strain response from FE-analysis.



(b) Damage distribution at peak-stress.

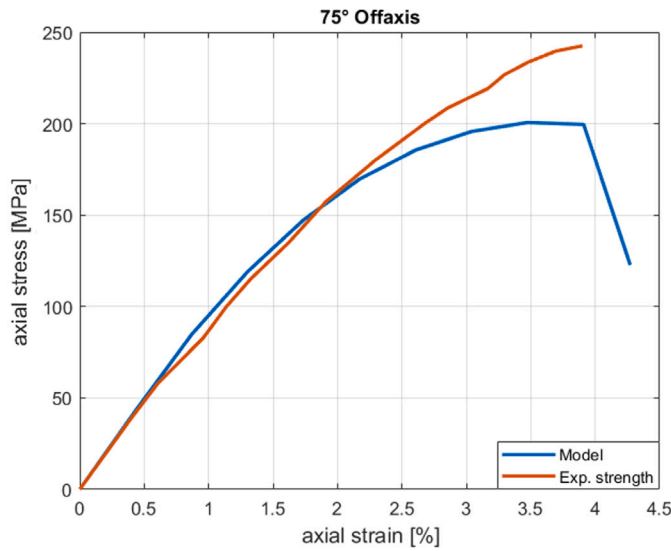
**Fig. 12.** (a) FE-analysis of the UD-ply specimen for 60° off-axis loading, (Koerber and Camanho, 2011). (b) Shear-splitting failure mode with damage. (SDV1 is the damage variable  $\alpha$ .)

that the width over hole diameter ratio is five. The results for these coupons show a good correlation with the experimental results. This is evidenced by the fact that the same percentage deviation is obtained in the two different thicknesses (2%).

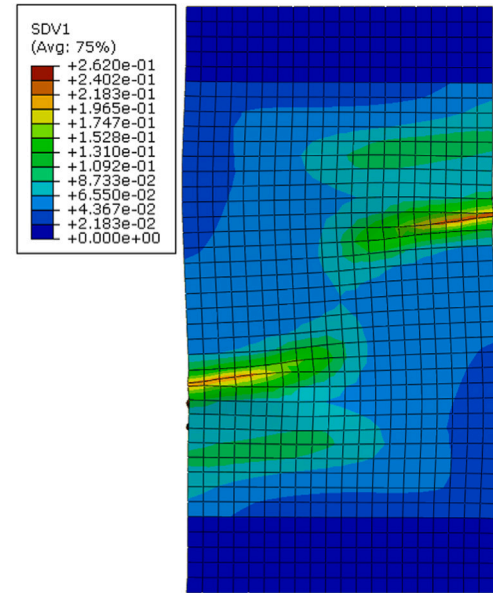
According to Wisnom et al. (2010), driven by kink-band formation in the 0° plies, the sub-laminate scaled notched specimens fail with a brittle failure mechanism as failure mode. We can trace the crack propagation from the deleted elements in the 0° ply; Fig. 18(b) shows the crack propagation in the 4 mm thick case. In the pre-peak response, the crack follows a path longitudinal to the applied load in the same way as the brittle mechanism up to the peak-load. Post-peak, the crack starts to follow a 45° oriented direction. The same failure mechanism is observed also in the 4 mm thick specimen.

### 3.4.3. In-plane size effects

From the experimental results of the 4 mm thick case in Table 4, it is noted that the strength of the material is affected by a size effect driven by the in-plane stress response of the specimens. A drop of 19% of the strength is observed when the hole diameter is increased from 6.35 mm (32 mm×32 mm specimen) to 25.4 mm (128 mm×128 mm specimen). Lee and Soutis (2008) attributes this reduction to the hole size effect in a finite width specimen. Despite the fact that the stress concentration factors around the hole are constant due to the same width over hole diameter ratio, the stress distribution across the specimen width is dependent on the hole size. This is due to the fixed damage zone described by the damage evolution rule (24), in particular, related to

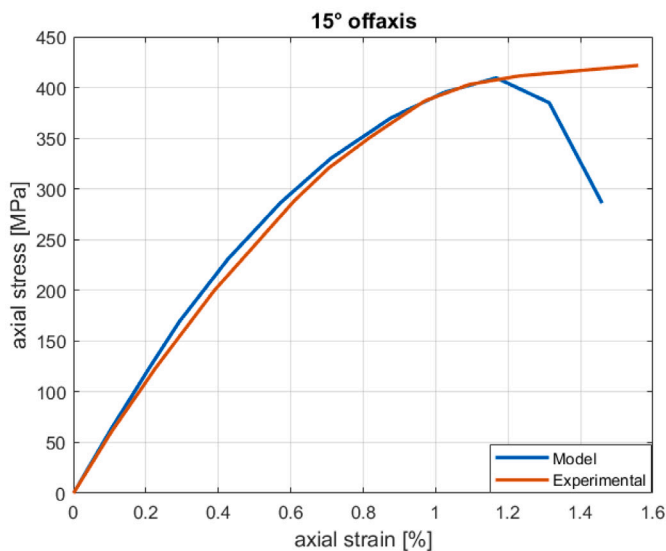


(a) Stress-strain response from FE-analysis.

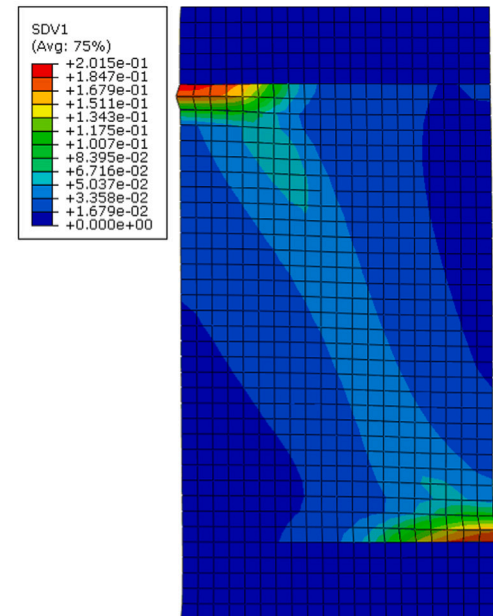


(b) Damage distribution at peak-stress.

**Fig. 13.** (a) FE-analysis of the UD-ply specimen for 75° off-axis loading, (Koerber and Camanho, 2011). (b) Shear-splitting failure mode with damage. (SDV1 is the damage variable  $\alpha$ .)



(a) Stress-strain response from FE-analysis.



(b) Damage distribution at peak-stress.

**Fig. 14.** (a) FE-analysis of the UD-ply specimen for 15° off-axis loading, (Koerber and Camanho, 2011). (b) Shear-splitting/kink-band failure mode with damage. (SDV1 is the damage variable  $\alpha$ .)

the fixed  $l_c$ -parameter. As the specimen becomes larger, more elastic energy is stored, corresponding to larger damage driving energy  $\mathcal{A}$ . This contributes to more intense damage evolution and an earlier failure as compared the smaller hole diameters.

From the simulation point of view, increasing the in-plane dimension while keeping the same element diameter leads to a dramatic increase of the degrees of freedom. Hence, in order to avoid overly demanding computations, the simulations are conducted with intermediate values of the hole diameters. To this end, analyses for hole

diameters 8 mm (40 mm×40 mm specimen dimensions) up to 10 mm (50 mm×50 mm) are carried out. The results are shown in Fig. 19. A clear decreasing trend in the material strength is observed. Using linear extrapolation, the strength for the 12.7 mm hole diameter is predicted to 306 MPa, which deviates from the experimental results by 1.6%. This linear extrapolation does not work to predict the strength for the 25.4 mm hole diameter case. This would yield a peak-stress of 192 MPa, corresponding to 32% difference from the experimental result. In Fig. 19, the analytical result for a stress concentration around



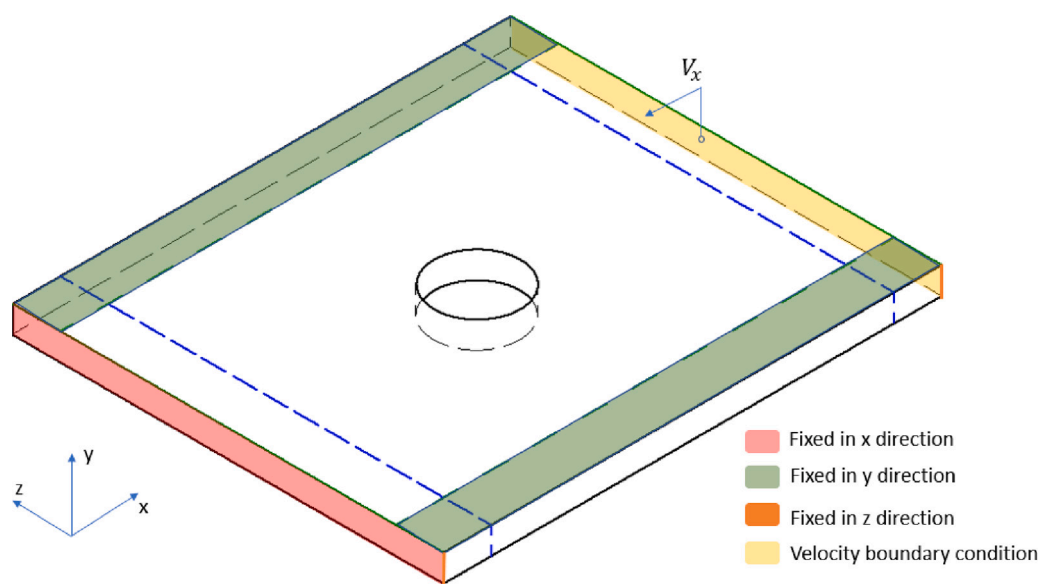
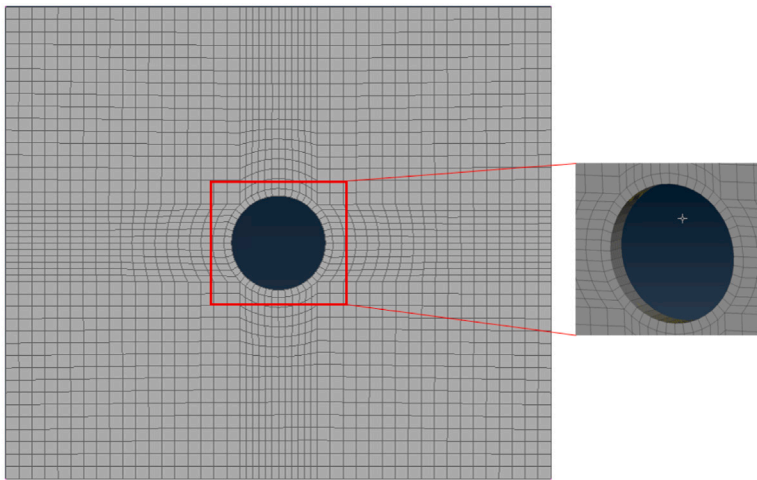
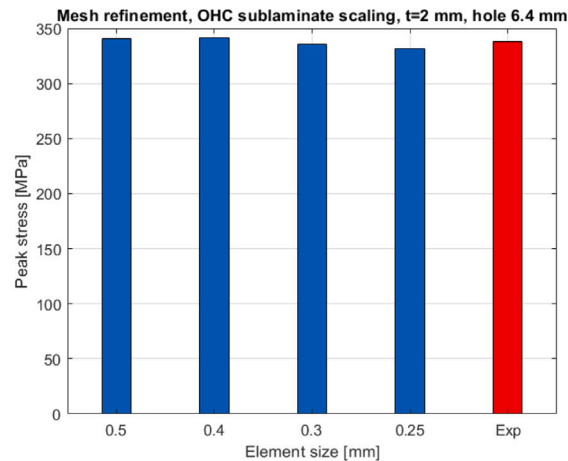


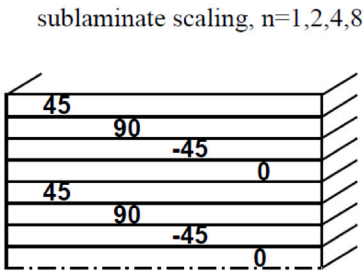
Fig. 15. Boundary condition of the model.



(a) Mesh of the OHC-laminate



(b) Predicted peak-stresses for the 2mm thick notched sub-laminate scaled specimen for different mesh sizes



(c) Sub-laminate stacking sequence.

Fig. 16. FE-discretization of the open hole sub-laminate stacked specimen.



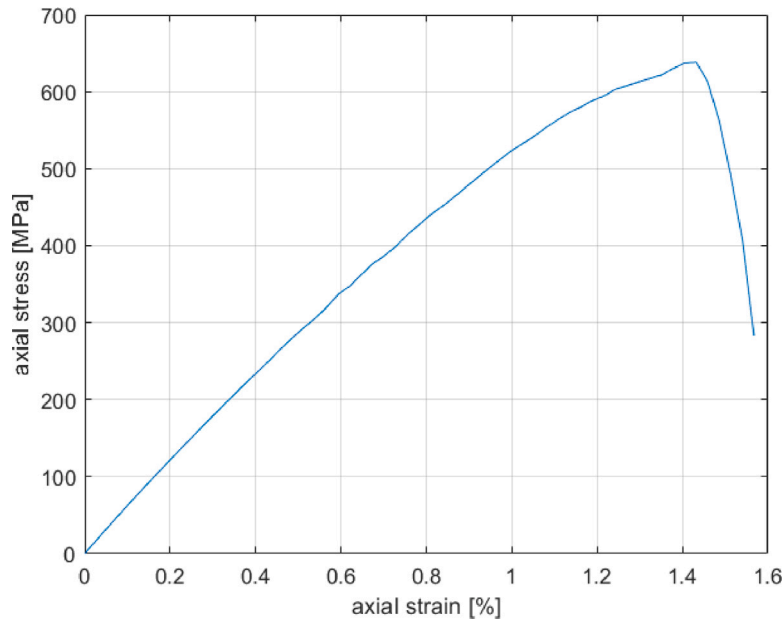


Fig. 17. Stress-strain response from FE-analysis of the un-notched 2 mm thick sub-laminate scaled specimen.

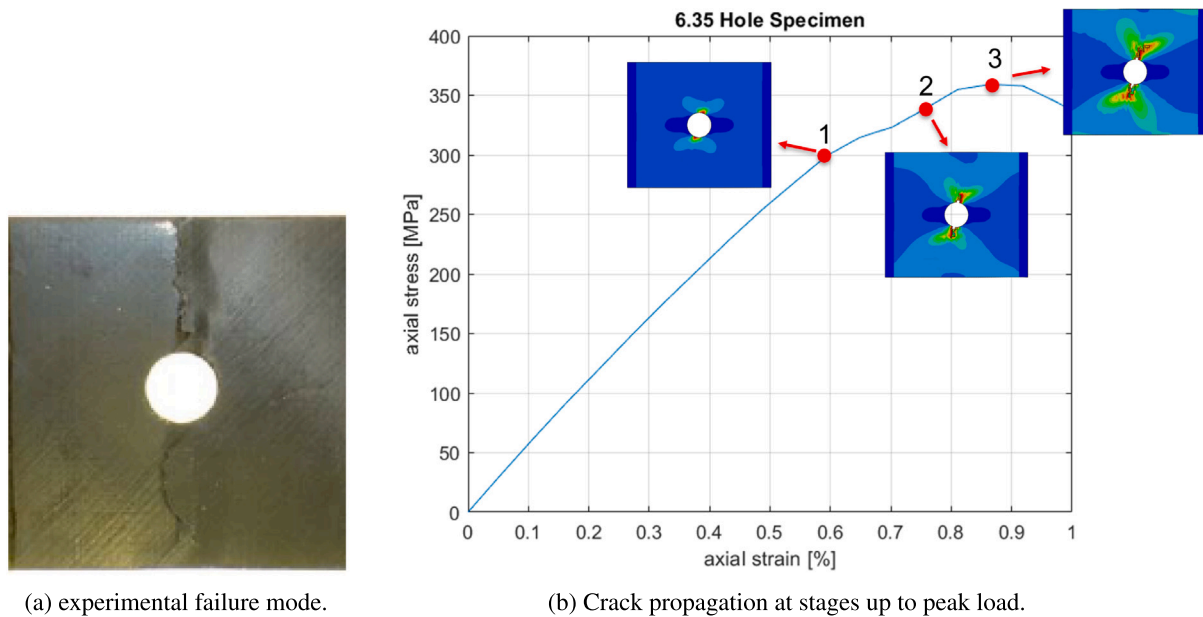


Fig. 18. Crack propagation during (vertical) compressive loading in the  $0^\circ$ -ply of the sub-laminate scaled 6.35 mm hollow specimen. The laminate thickness is 4 mm corresponding to 32plies. Experimental results showing brittle failure is by Wisnom et al. (2010).

hole is included. That concentration factor is 3 for the compressive far field stress for elastic isotropy. Considering the un-notched strength for the 4 mm laminate, one obtains from Table 4 the strength  $681/3 = 227$  MPa, corresponding to completely brittle fracture when failure process zone is negligible. This is roughly in-line with the experimental strength 280 MPa for the largest hole sizes in Table 4.

#### 4. Concluding remarks

A continuum damage model that can predict fiber kinking response for compressive loaded UD-ply has been further developed in context

of multidirectional laminated structures. The model gives a mesh objective response, also reported herein for the ply-level response. The extension to describe kink-band formation with misaligned fibers on the subscale has been presented. The model behavior was demonstrated for  $0^\circ$ -loaded plies (with  $5^\circ$  misalignment) for pure kink-band formation, whereas shear splitting (or matrix shear failure) is obtained for “larger” off-axis loading. Here, it is noted that the range of off-axis loading angles with kink-band failure is still an open question.

FE-validation at the ply-level gives good results for the pre-peak behavior for the considered off-axis angles. In the validation of the OHC-test, sub-laminate scaling was considered. Reasonable results for

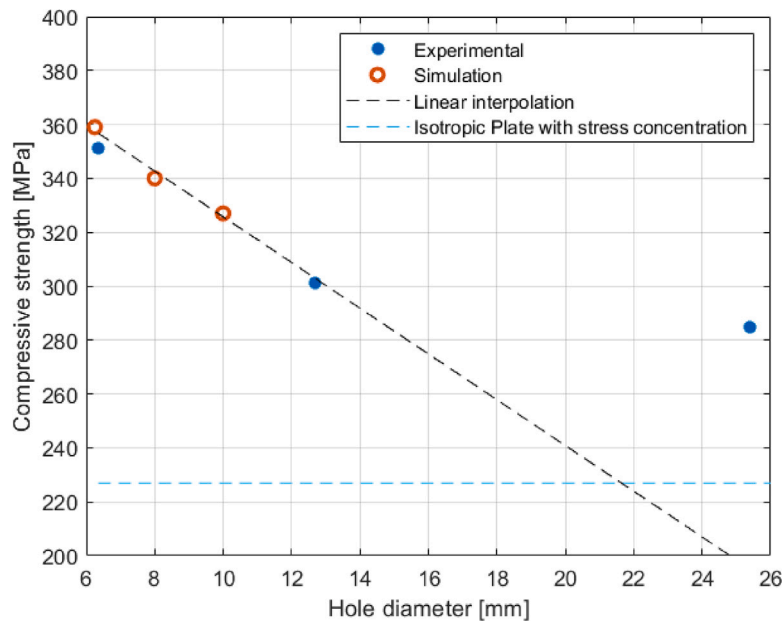


Fig. 19. Experimental and simulated in plane size effect on strength of the laminate. Linear interpolation is used for a prognosis of up to 12.7 mm hole case. The limiting case of completely brittle fracture, without influence of damage progression, is included by the dotted horizontal line. The thickness of the laminate is 4 mm.

the failure stresses were obtained for the different hole diameters. We also verified the experimentally observed “brittle” failure mode, dominated by intra-laminar kink-band failure for the  $0^\circ$ -loaded plies. The results also exhibit a size effect with a reduced failure stress for increasing hole diameters. More simulation results are needed to study the response of the OHC specimens in the 12.7–25.4 mm range.

#### CRedit authorship contribution statement

**Ragnar Larsson:** Conceptualization, Formal analysis, Supervision, Writing – review & editing. **Giovanni Brambati:** Software, Data curation, Visualization, Writing – original draft. **Renaud Gutkin:** Supervision, Validation, Writing – review & editing.

#### Declaration of competing interest

The authors declare that they have no known competing financial interests or personal relationships that could have appeared to influence the work reported in this paper.

#### Data availability

Data will be made available on request.

#### References

- Benzeggagh, M., Kenane, M., 1996. Measurement of mixed-mode delamination fracture toughness of unidirectional glass/epoxy composites with mixed-mode bending apparatus. *Compos. Sci. Technol.* 56 (4), 439–449.
- Bru, T., Hellström, P., Gutkin, R., Ramantani, D., Peterson, G., 2016. Characterisation of the mechanical and fracture properties of a uni-weave carbon fibre/epoxy non-crimp fabric composite. *Data Brief* 6, 680–695.
- Camanho, P., Davila, C., 2002. Mixed-mode decohesion finite elements for the simulation of delamination in composite materials.
- Chen, B., Tay, T., Baiz, P., Pinho, S., 2013. Numerical analysis of size effects on open-hole tensile composite laminates. *Composites A* 47, 52–62.
- Costa, S., Gutkin, R., Olsson, R., 2017. Mesh objective implementation of a fibre kinking model for damage growth with friction. *Compos. Struct.* 168, 384–391.
- Fleck, N., Deng, L., Budiansky, B., 1995. Prediction of kink width in compressed fiber composites. *J. Appl. Mech.* 62 (2), 329–337.

- Grauers, L., Olsson, R., Gutkin, R., 2014. Energy absorption and damage mechanisms in progressive crushing of corrugated NCF laminates: Fractographic analysis. *Compos. Struct.* 110, 110–117.
- Gutkin, R., Costa, S., Olsson, R., 2016. A physically based model for kink-band growth and longitudinal crushing of composites under 3D stress states accounting for friction. *Compos. Sci. Technol.* 135, 39–45.
- Herraez, M., Bergan, A., Gonzalez, C., Lopes, C., 2018. Modeling fiber kinking at the microscale and mesoscale. *NASA/TP-2018-220105*.
- Jensen, H., Christoffersen, J., 1997. Kink band formation in fiber reinforced materials. *J. Mech. Phys. Solids* 45 (7), 1121–1136.
- Koerber, H., Camanho, P., 2011. High strain rate characterisation of unidirectional carbon-epoxy IM7-8552 in longitudinal compression. *Composites A* 42, 462–470.
- Larsson, R., Gutkin, R., Rouhi, M., 2018. Damage growth and strain localization in compressive loaded fiber reinforced composites. *Mech. Mater.* 127, 77–90.
- Lee, J., Soutis, C., 2008. Measuring the notched compressive strength of composite laminates: Specimen size effects. *Compos. Sci. Technol.* 68 (12), 2359–2366.
- Deformation and Fracture of Composites: Analytical, Numerical and Experimental Techniques, with regular papers.
- Leone, Jr., F.A., 2015. Deformation gradient tensor decomposition for representing matrix cracks in fiber-reinforced materials. *Composites A* 76, 334–341.
- Miehe, C., Schröder, J., Schotte, J., 1999. Computational homogenization analysis in finite plasticity. Simulation of texture development in poly-crystalline materials. *Comput. Methods Appl. Mech. Engrg.* 171, 387–418.
- Pimenta, S., Gutkin, R., Pinho, S., Robinson, P., 2009. A micromechanical model for kink-band formation: Parts I-II. *Compos. Sci. Technol.* 69 (7–8), 948–955.
- Pinho, S., Iannucci, L., Robinson, P., 2014. Physically-based failure models and criteria for laminated fibre-reinforced composites with emphasis on fibre kinking: Part I: Development. *Composites A* 37 (1), 63–73.
- Smith, M., 2009. ABAQUS/Standard User's Manual, Version 6.9. Dassault Systemes Simulia Corp.
- Suquet, P., 1985. Local and global aspects in the mathematical theory of plasticity. In: Sawczuk, A., Bianchi, G. (Eds.), *Plasticity Today: Modelling, Methods and Applications*. Elsevier Applied Science Publishers, London, pp. 279–310.
- Turon, A., Dávila, C., Camanho, P., Costa, J., 2007. An engineering solution for mesh size effects in the simulation of delamination using cohesive zone models. *Eng. Fract. Mech.* 74.
- Wilhelmsson, D., Gutkin, R., Edgren, F., Asp, L., 2018. An experimental study of fibre waviness and its effects on compressive properties of unidirectional NCF composites. *Composites A* 107, 665–674.
- Wisnom, M., Hallett, S., Soutis, C., 2010. Scaling effects in notched composites. *J. Compos. Mater.* 44 (2), 195–210.
- Zhou, S., Sun, Y., Ridha, M., Chen, B., Tay, T., 2017. Progressive damage simulation of scaling effects on open-hole composite laminates under compression. *J. Reinf. Plast. Compos.* 36.